A continuous cost–efficiency spectrum governs brain-wide communication and cognitive reconfiguration

Kaining Peng[1†], Zixiang Luo[1,2†], Zhu Zhuo[1,3], Shengyuan Cai[1,4], Yinuo Zhang[1], Quanying Liu[1*]

[1]Department of Biomedical Engineering, Southern University of Science and Technology, Shenzhen, 518055, China.
[2]Division of Life Science, The Hong Kong University of Science and Technology, Hong Kong SAR, 999077, China.
[3]Department of Biomedical Engineering, National University of Singapore, Singapore, 119276, Singapore.
[4]Neuroscience Research Center, Charité – Universitätsmedizin Berlin, Corporate Member of Freie Universität Berlin and Humboldt-Universität zu Berlin, Berlin, 10117, Germany.

*Corresponding author(s). E-mail(s): liuqy@sustech.edu.cn;
†These authors contributed equally to this work.

Abstract

Information communication in the brain must balance efficient functional integration with the metabolic and physical costs of long-range connectivity. How this cost–efficiency balance is implemented in large-scale communication networks, and how it adapts across cognitive states and pathology, remains poorly understood. In this study, by systematically tuning the strength of distance constraints in a dynamical model, we revealed a continuum of effective connectivity (EC) architectures, ranging from localized low-cost architectures to globally integrated high-efficiency configurations. We show that large-scale brain communication is organized along a continuous cost–efficiency trade-off spectrum, which serves as a latent scaffold for flexible network reconfiguration across cognitive states. Empirical resting EC occupies a balanced region on this spectrum, near a knee point where cost is already substantially reduced without a comparably large loss of efficiency. Cognitive task engagement

dynamically shifts the brain's operating point along the same spectrum, toward higher-cost, higher-efficiency regimes through enhanced between-network interactions. In major depressive disorder, this state-dependent reorganization is blunted, revealing an impaired access to higher-efficiency regimes. Together, these findings suggest that cognitive flexibility and dysfunction are governed not merely by discrete network states, but by constrained navigation along a continuous cost–efficiency spectrum, providing a unifying framework for interpreting brain-wide communication and its reconfiguration.

1 Introduction

Flexible cognition requires the human brain to coordinate communications across widely distributed regions. However, such brain-wide communication is constrained by energetic and physical limitations [1]. Long-range communications facilitate global integration but require substantial metabolic and wiring resources, while local interactions are more economical but limited in functional reach [2–4]. This tension gives rise to the fundamental cost–efficiency trade-off that shapes large-scale brain network organization. Importantly, it remains unclear whether this trade-off reflects a fixed operating point or a dynamically reconfigurable property of brain networks. Given the need to adapt to varying cognitive states, task demands, and levels of internal engagement, we hypothesize that the brain may flexibly reposition itself within a constrained space of communication networks, transiently prioritizing global integration or local efficiency while remaining embedded within a stable anatomical scaffold [5–11]. Exploring such reconfiguration requires moving beyond static descriptions of observed connectivity to characterize the range of interaction architectures accessible to the brain under biophysical constraints.

Existing methods for brain network analysis, including structural connectivity (SC) and functional connectivity (FC), offer valuable insights but remain incomplete in characterizing the full space of brain communication architectures [12]. SC maps the anatomical wiring of the brain and reveals how physical distance and wiring economy constrain network organization [13, 14]. However, it is inherently static and cannot capture how communication patterns adapt across cognitive states. FC, on the other hand, identifies state-dependent statistical dependencies between brain regions, uncovering properties like modularity, hierarchy, and small-world organization [15–20]. While FC provides valuable descriptions of observed patterns in specific states, it does not offer a continuous space of possible communication networks or reveal how the brain transitions between them [5, 21, 22]. Consequently, they primarily describe only "what is" in terms of observed brain connectivity; both SC and FC are limited in answering "what if" questions—how brain communication could reorganize under different constraints. To fully understand the brain's flexible

communication, we need an approach that can explore intermediate regimes and counterfactual network states across different conditions [14, 23].

Answering such "what if" questions require moving beyond static network descriptions to an interpretable dynamical modeling framework [24]. Such framework should do more than summarize the connectivity pattern expressed in a given state; it should be able to identify alternative network configurations that remain consistent with empirical data and reveals the dynamical rules governing large-scale communication. This allows for counterfactual "what if" exploration, enabling us to assess how changes in spatial embedding or coupling structure would reshape network organization and its cost–efficiency trade-off. However, no systematic framework has yet been developed to map these data-consistent communication networks. In this study, we introduce a distance-constrained linear dynamical model that captures brain dynamics and infers brain-wide effective connectivity (EC) from data (Fig. 1a–c) [25–28]. By embedding a tunable spatial distance constraint into the model, we uncover a continuum of plausible brain network configurations (Fig. 1d) and facilitates counterfactual mapping of how brain network organization shifts along a continuous cost–efficiency trade-off spectrum (Fig. 1e).

On the spectrum, we identify the position of empirical brain network by comparing model-derived EC with an independent whole-brain EC benchmark [25]. We found that the human brain operates at an intermediate point along the cost-efficiency spectrum, balancing low communication cost with high efficiency (Fig. 1e). When comparing the empirical network with the Pareto front, we observed that it lies close to, but does not strictly coincide with, Pareto-optimal solutions (Fig. 1f). This suggests that brain networks are not purely optimal for cost–efficiency trade-off. Instead, we show that brain also retains additional properties such as robustness and modularity, which may support reliable and flexible computation (Fig. 1g). Furthermore, across cognitive states, task engagement shifts the brain's operating point within the same cost–efficiency landscape, moving towards higher-cost, higher-efficiency regimes, suggesting a dynamic reallocation of communication resources in response to cognitive demands (Fig. 1h). Together, these results support a view of cost–efficiency not as a single optimal solution, but as a constrained landscape that the brain dynamically navigates to support flexible cognition.

2 Results

2.1 A distance-constrained linear dynamical model captures brain dynamics and EC

To characterize how spatial constraints shape large-scale brain communication and contribute to the cost–efficiency trade-off, we introduce a distance-constrained linear dynamical model that estimates whole-brain EC while explicitly accounting for physical distance. This model predicts regional blood oxygenation level dependent (BOLD) activity at each timepoint via a weighted

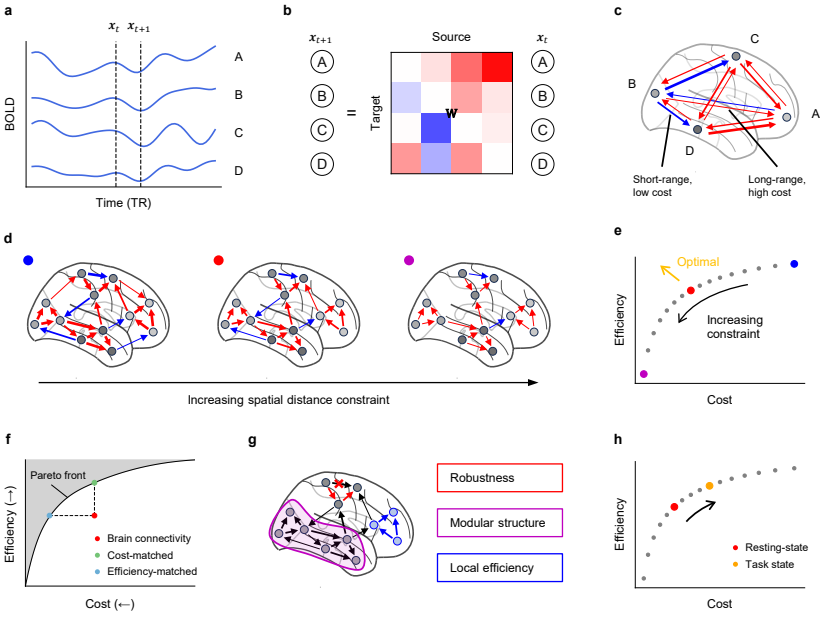

Fig. 1 Framework for examining cost–efficiency trade-off in large-scale brain networks. a, Regional BOLD signals extracted from resting-state fMRI data. **b**, Linear autoregressive model estimating the effective connectivity matrix $\boldsymbol{W}$, capturing directional interactions between brain regions. **c**, Brain regions embedded in 3D anatomical space, with connections constrained by spatial distance. **d**, Connectivity patterns under increasing spatial distance constraint. Stronger constraint yields more localized connectivity. **e**, Trade-off curve between communication cost and efficiency across different constraint levels. **f**, Cost–efficiency Pareto front with human brain networks compared to Pareto-front synthetic networks matched to human cost or efficiency. **g**, Additional graph-theoretical metrics for comparing human brain networks with Pareto-front networks. **h**, Cost–efficiency trade-off across resting and task states with task-related rebalancing of communication cost and efficiency.

connectivity matrix $\boldsymbol{W}$, with a single parameter λ governing the strength of spatial distance regularization (Fig. 1a–d; Methods).

We validated the model on resting-state fMRI data from 100 Human Connectome Project (HCP) participants (Fig. 2). At the individual level, the predicted BOLD signals closely tracked the empirical data (Fig. 2a), confirming that the model captures much of the large-scale temporal dynamics. We benchmarked the performance of ridge regularization by comparing it to sparse lasso regression across a range of λ values. While lasso showed comparable performance at low λ, its prediction accuracy dropped sharply as the spatial constraint increased (e.g., at $\lambda = 0.7$, mean $R^2 = 0.510$ for lasso vs. 0.744 for ridge). In contrast, ridge regression maintained stable performance across a wide range of λ values (mean $R^2 \geq 0.660$ for ridge across $\lambda \in [0.1, 0.9]$; Fig. 2b). Moreover, our distance-constrained model offered superior prediction performance compared to standard ridge regression (Supplementary Fig. 1). We thus used ridge regression with a spatial distance prior in subsequent analyses.

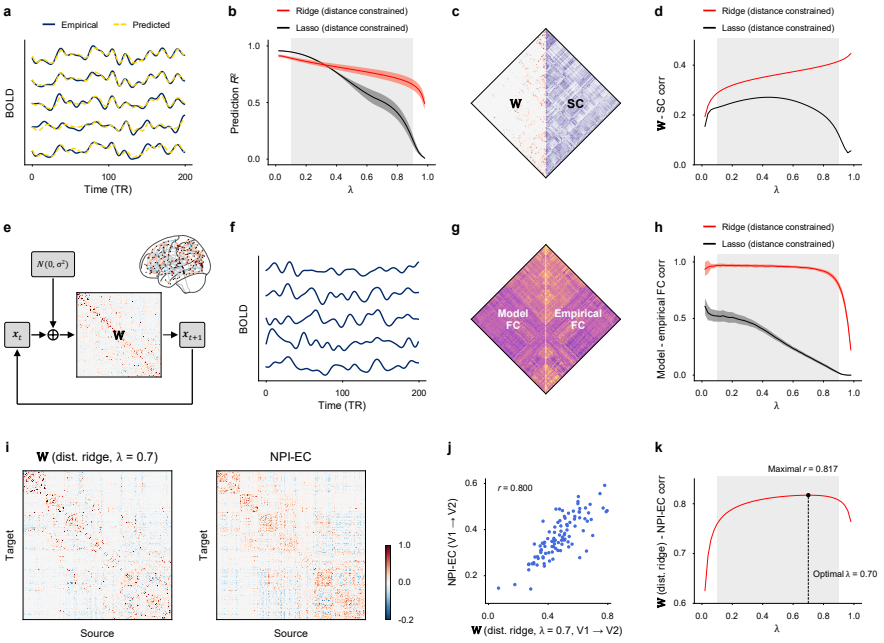

Fig. 2 A distance-constrained linear dynamical model captures brain dynamics and inter-regional relationships. **a**, Predicted and empirical BOLD signals at the individual level. Representative panels in **a**, **c**, and **e**–**g** are shown for distance-constrained ridge regression at $\lambda = 0.7$. **b**, Prediction performance across λ (5-fold cross-validation; mean ± s.d. across 100 participants). Ridge maintained stable prediction accuracy across λ. **c**, Estimated EC matrix $\boldsymbol{W}$ and SC at the group level ($r = 0.385$). **d**, Correlation between estimated $\boldsymbol{W}$ and SC across λ. Ridge showed consistently higher correlation with SC than lasso. **e**, Continuous generation of synthetic BOLD signals from estimated $\boldsymbol{W}$. **f**, Synthetic BOLD signals at the individual level. **g**, Model FC and empirical FC matrices at the individual level ($r = 0.957$). **h**, Model–empirical FC correlation across λ (mean ± s.d. across 100 participants). Ridge achieved high FC reconstruction accuracy across λ. **i**, Estimated EC matrix $\boldsymbol{W}$ and NPI-EC at the group level ($\lambda = 0.7$). **j**, Correlation between estimated EC matrix $\boldsymbol{W}$ at $\lambda = 0.7$ and NPI-EC for the V1→V2 connection at the individual level ($r = 0.800$). **k**, Correlation between estimated EC matrix $\boldsymbol{W}$ and NPI-EC across λ, peaking at $\lambda = 0.7$. Corr, correlation.

Next, we examined whether the estimated EC matrix $\boldsymbol{W}$ captures meaningful inter-regional organization rather than serving purely as a forecasting tool. Structurally, $\boldsymbol{W}$ exhibited a distance-dependent organization, with increased correspondence to SC as the spatial constraint strengthened (for ridge, from $r = 0.288$ at $\lambda = 0.1$ to $r = 0.416$ at $\lambda = 0.9$; Fig. 2c–d). Functionally, synthetic BOLD signals generated from the estimated $\boldsymbol{W}$ closely reproduced temporal fluctuations observed in the data (Fig. 2e–f), and the FC derived from these synthetic signals matched empirical FC at the individual level (mean model–empirical FC correlation $r \geq 0.798$ for ridge across $\lambda \in [0.1, 0.9]$; Fig. 2g–h). This high degree of FC reconstruction was not observed in control analyses based on simulated dynamics (Supplementary Fig. 2) or a matched null model (Supplementary Fig. 3). The concurrent

increase in SC correspondence (Fig. 2c–d) and consistently high FC reconstruction across λ (Fig. 2g–h) suggest that strengthening the spatial prior redistributes directed interactions under distance constraints while preserving the large-scale statistical scaffold of brain activity.

To identify the operating point of the empirical brain network within this spectrum, we compared the EC estimated from our model at various λ values against an independent EC benchmark (NPI-EC) (Fig. 2i). At the individual level, we identified that the estimated EC matrix captured variation in connection strength similar to NPI-EC (e.g., $r = 0.800$ for the V1→V2 connection; Fig. 2j). Similar correspondence was observed across additional connections (Supplementary Fig. 4). At the group level, the correlation peaked at $\lambda = 0.7$ ($r = 0.817$; Fig. 2k), and this peak was reproducible across fMRI datasets (Supplementary Fig. 5). These results indicate that this value of λ provided the best approximation of human brain EC. We thus used the EC obtained from the distance-constrained linear dynamical model at $\lambda = 0.7$ as the empirical EC for subsequent analyses.

2.2 Cost–efficiency trade-off spectrum of brain communication networks

We next examined how EC patterns reorganize as the spatial constraint parameter λ increases (Fig. 3a–b). As λ increased, the estimated connectivity shifted from a more distributed to a more localized structure. At smaller values of λ, strong connections spanned long distances, while larger values weakened these long-range links and formed denser local clusters (Fig. 3b; Supplementary Fig. 6). Interestingly, despite this attenuation of long-range links, some, such as the connection from the posterior cingulate cortex (PCC) to the anterior cingulate cortex (ACC), were preserved even under stronger spatial constraints (Fig. 3a).

We then assessed the impact of these reorganizations on network communication by evaluating communication cost and functional efficiency across λ (Methods). Increasing λ consistently reduced communication cost (Fig. 3c), but also decreased functional efficiency (Fig. 3d), revealing a cost–efficiency trade-off spectrum (Fig. 3e). This relationship was notably altered in a spatially shuffled null model that disrupts anatomical embedding (Supplementary Fig. 7), confirming that the trade-off is intrinsic to human brain EC, not merely an artifactual result of stronger regularization. To test the robustness of these findings, we replicated the analysis in an independent Chinese Human Connectome Project (CHCP) cohort, obtaining similar results (Fig. 3f–h). We also observed an increase in small-worldness and modularity with higher λ (Supplementary Fig. 8), consistent with the denser local clustering at larger values of λ.

As λ increased, the cost–efficiency spectrum bent toward the upper-left, forming a knee region in the curve (Fig. 3e). The empirically observed $\lambda = 0.7$ lies near this knee, where communication cost has been significantly reduced without a large loss in functional efficiency compared to more extreme

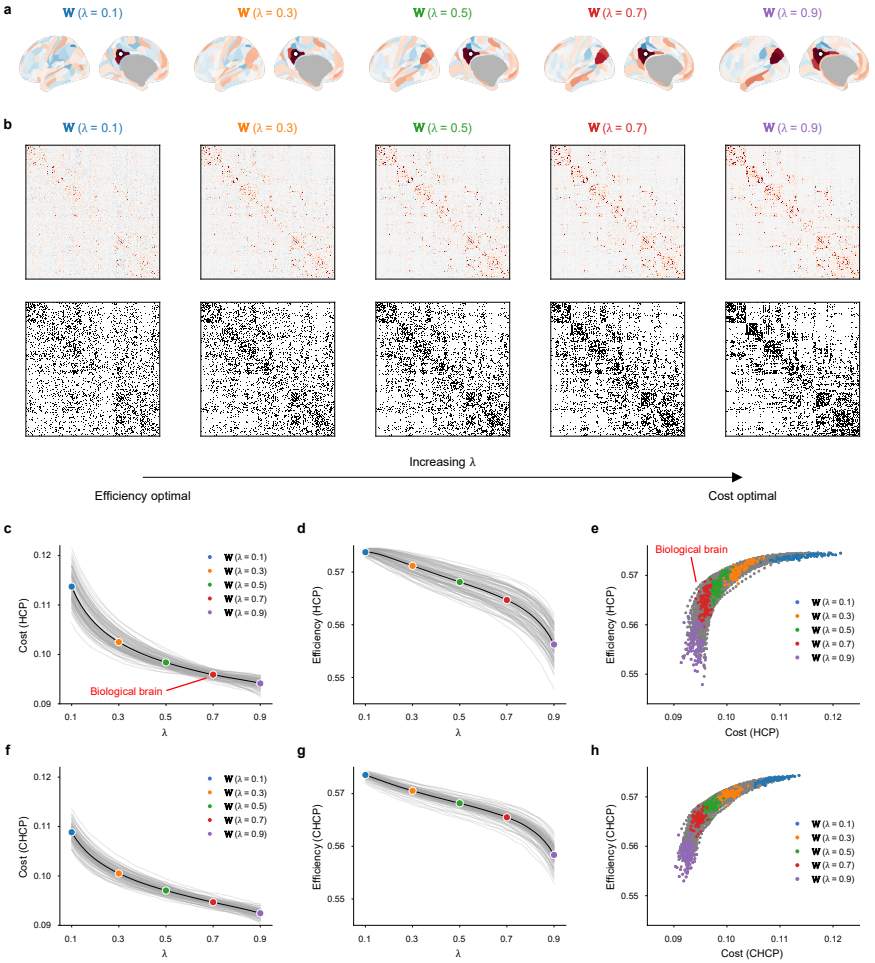

Fig. 3 Changes in communication cost and functional efficiency with increasing spatial distance constraint. a, Example of seed-based EC from PCC to other brain regions under different λ values. With increasing λ, the seed-based EC becomes more spatially localized while preserving selective long-range links. **b**, Example of whole-brain EC matrices and their corresponding binarized adjacency matrices (thresholded at the top 15%) under different λ values. With increasing λ, the estimated connectivity becomes more modular. **c**–**e**, Communication cost (**c**), functional efficiency (**d**), and cost–efficiency spectrum (**e**) as a function of λ in 100 HCP participants. Empirical EC ($\lambda = 0.7$) lies near a knee of the spectrum, consistent with a balanced cost–efficiency organization. **f**–**h**, Replication of **c**–**e** in an independent sample of 100 CHCP participants. Gray lines show individual participants, and the black curve shows the group mean.

constraint regimes. Consistent with this pattern, derivatives of communication cost and functional efficiency with respect to λ further highlight that beyond this point, cost reductions exhibit diminishing returns while efficiency decreases sharply (Supplementary Fig. 9). These findings confirm that human brain EC is organized along a cost–efficiency trade-off spectrum, with the empirical brain network residing near the knee of the trade-off curve.

2.3 Brain networks exhibit higher within-network efficiency and robustness than Pareto-optimal networks

To investigate whether the empirical brain network operates near an attainable boundary in the cost–efficiency space, we compared the estimated EC to the Pareto-front solutions derived using a multi-objective genetic algorithm (GA) (Fig. 4a; Methods). The Pareto front is the upper-left boundary of attainable solutions in the cost–efficiency space, where no network can improve one objective (cost or efficiency) without worsening the other. Our results show that the potential brain networks derived from our distance-constrained linear dynamical model lie close to this GA-derived Pareto front (Fig. 4b), indicating that the empirical EC ($\lambda = 0.7$) operates near the attainable frontier of joint cost reduction and efficiency preservation. Although visual inspection suggests that the empirical EC is near the Pareto front, it does not quantify where the network lies within the attainable landscape, nor does it distinguish between balanced compromises and solutions that prioritize one objective over the other. To address this, we introduced the "Optimization Degree", a quantitative measure of proximity to the Pareto front (Methods). Brain networks show consistently high Optimization Degree values across a broad range of λ (mean Optimization Degree optdeg ≥ 0.847 across $\lambda \in [0.1, 0.9]$; Fig. 4c), demonstrating that the estimated EC remains close to the attainable boundary. The Optimization Degree peaked at $\lambda = 0.72$ (optdeg $= 0.887$; Fig. 4c), closely aligning with the empirically selected $\lambda = 0.7$, which corresponds to maximal agreement with the NPI-EC. A highly consistent pattern was shown in an independent CHCP cohort, with the peak occurring at $\lambda = 0.78$ (Supplementary Fig. 10). These findings suggest that the brain network operates in a balanced region of the trade-off spectrum, optimizing both cost and efficiency at an intermediate λ.

Despite the empirical EC being close to the Pareto front, it does not coincide exactly with it. To explore potential network properties that could account for this offset, we selected three representative Pareto-front networks for comparison: a cost-matched Pareto network, an efficiency-matched Pareto network, and an optimal Pareto network with the highest Optimization Degree (Fig. 4d). Empirical EC showed substantial overlap with these Pareto networks at the level of overall connectivity pattern (Fig. 4e), suggesting that they provide a meaningful basis for further functional comparison. On this basis, we assessed how these networks compare in terms of communication efficiency within and between functional modules. Relative to the Pareto references, empirical EC achieved higher within-network efficiency (+10.4%, +8.8%, +9.1% relative to the cost-matched, efficiency-matched, and optimal Pareto networks, respectively), with only a modest reduction in between-network efficiency (−4.0%, −1.7%, −0.5% relative to the same networks; Fig. 4f–g). Notably, the within-network efficiency advantage of empirical EC extends across the Pareto front, surpassing the efficiency-matched and optimal

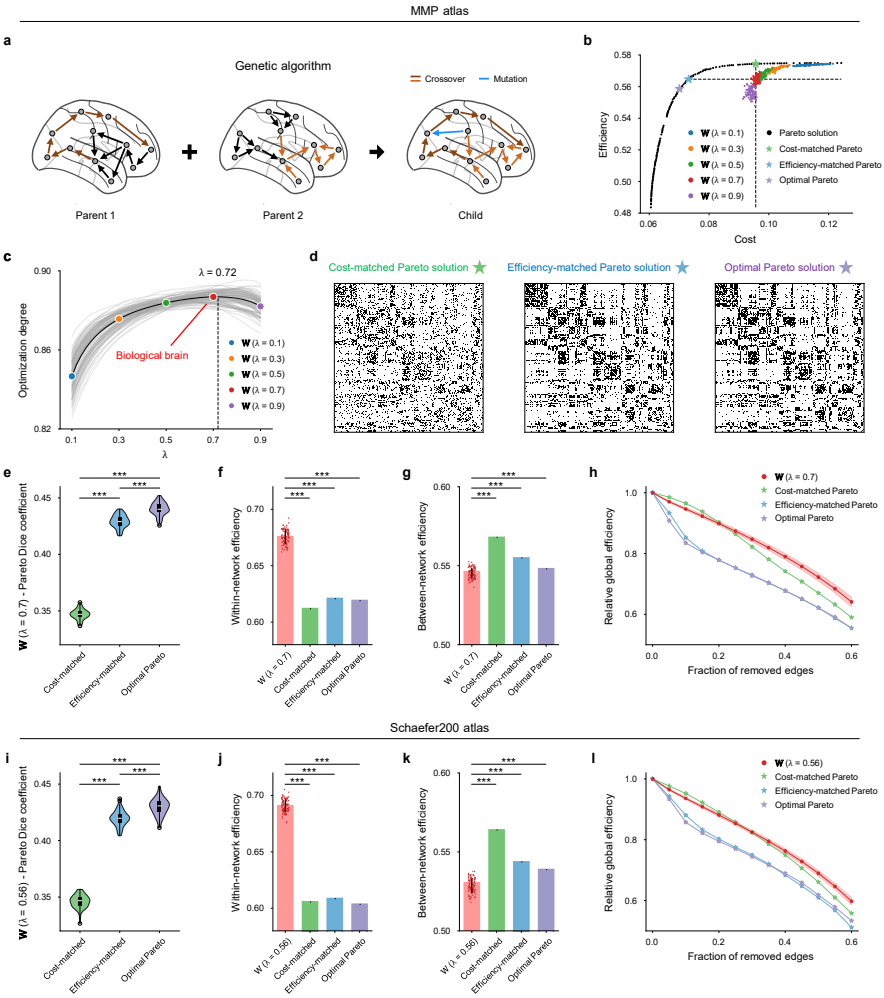

Fig. 4 Comparison between human EC and Pareto-front solutions from a genetic algorithm. a, One genetic evolution step in the genetic algorithm, where a child is produced by inheriting a subset of connections from each parent and introducing additional randomly mutated connections. **b**, Trade-off locations of estimated EC and Pareto-front solutions in cost–efficiency space. Estimated EC lies close to the Pareto front. **c**, Optimization degree across λ, with the mean peaking at $\lambda = 0.72$, close to the empirically selected $\lambda = 0.7$. Gray lines show individual participants, and the black curve shows the group mean. **d**, Visualization of the cost-matched, efficiency-matched, and optimal Pareto networks. **e**, Dice coefficient between empirical EC and three representative Pareto-front networks. Empirical EC showed the highest overlap with the optimal Pareto network (all three comparisons: $P_{\mathrm{adj}} = 1.2 \times 10^{-17}$). **f**, Higher within-network efficiency in empirical EC than in three representative Pareto-front networks (all three comparisons: $P_{\mathrm{adj}} = 1.2 \times 10^{-17}$). **g**, Slightly lower between-network efficiency in empirical EC than in three representative Pareto-front networks (comparisons with cost-matched and efficiency-matched: $P_{\mathrm{adj}} = 1.2 \times 10^{-17}$; comparison with optimal: $P_{\mathrm{adj}} = 6.5 \times 10^{-10}$). **h**, Greater robustness of empirical EC to targeted edge removal than the efficiency-matched and optimal Pareto networks. **i–l**, Replication of **e–h** in the same participants using the Schaefer200 atlas (empirically selected $\lambda = 0.56$). Unless otherwise stated, box plots show the median (center line) and interquartile range (box), with whiskers extending from the quartiles to the most extreme data points within 1.5×IQR and fliers denote data points beyond the whiskers; bar plots and line plots show mean values and error bars indicate s.d. P_{adj} values were obtained using two-sided Wilcoxon signed-rank test with Bonferroni correction, $n = 100$. ***, $P_{\mathrm{adj}} < 0.001$.

Pareto networks, which are located near the upper part of within-network efficiency on the front (Supplementary Fig. 11). These results imply that, beyond a two-objective cost–efficiency criterion, human EC preferentially supports efficient within-network communication while retaining substantial cross-network coupling.

We further assessed robustness to edge removal by progressively removing edges ranked by importance and tracking the resulting global efficiency (Methods). Empirical EC demonstrated higher robustness than both the efficiency-matched and optimal Pareto networks, maintaining higher relative global efficiency after removing 10% of edges (i.e., 0.946 for empirical EC vs. 0.852 for efficiency-matched and 0.835 for optimal Pareto networks; Fig. 4h). Interestingly, the differences relative to the cost-matched Pareto network were modest. These findings indicate that Pareto solutions emphasizing cost and efficiency may be less robust, whereas empirical EC combines near-frontier cost–efficiency with greater resilience to targeted edge loss. These results were reproduced using the Schaefer200 atlas (Fig. 4i–l), confirming that these observations are not specific to a single spatial resolution. Overall, the empirical brain network does not merely optimize a single objective but occupies a balanced region of the trade-off space, where efficiency, cost, and robustness are jointly constrained.

2.4 Cognitive tasks drive the brain operating point toward higher efficiency

Cognitive demands are known to modulate brain effective connectivity [29], but whether this modulation systematically shifts brain networks along the cost–efficiency spectrum remains unclear. To address this, we tested whether cognitive tasks reposition whole-brain EC toward a regime of higher efficiency and higher cost compared to resting state. Using the HCP motor task, we first verified that the distance-constrained linear dynamical model remains predictive in task data (Fig. 5a), indicating that task-evoked BOLD dynamics can be captured within the same modeling framework. Additionally, task-state EC showed strong correspondence with SC across λ (Fig. 5b), confirming an anatomical scaffold for the task-state EC.

At $\lambda = 0.7$, we observed clear state-dependent reconfigurations in whole-brain EC, with shifts from resting state to motor-task state (Fig. 5c–d). Seed-to-whole-brain maps revealed strengthened couplings from a somatomotor seed to distributed targets during motor execution (Fig. 5c–d, upper right), and a dorsal-attention seed also showed enhanced coupling to motor cortex in motor-task state (Fig. 5c–d, lower right). Overall, motor execution involved a more distributed coupling profile, with stronger interactions extending beyond the local somatomotor areas to include cross-system connections.

Next, we quantified how these connection-level changes translate into shifts in the cost–efficiency landscape. Across participants, motor-task states shifted toward higher functional efficiency together with higher communication cost compared to rest ($P = 3.9 \times 10^{-18}$ for efficiency and $P = 8.2 \times 10^{-17}$ for

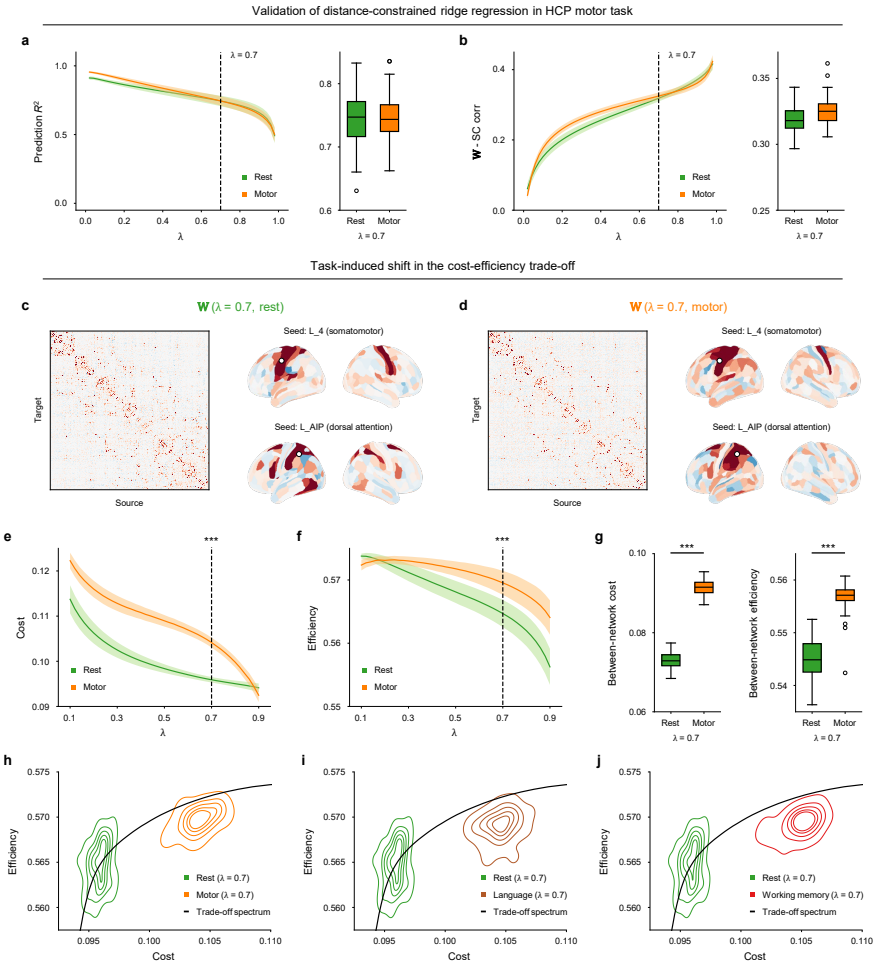

Fig. 5 Shifts of cost–efficiency trade-off points in cognitive task states. a, Comparable next-step prediction performance across λ in resting and motor task states, capturing short-term temporal evolution in both states. **b**, Comparable EC–SC correspondence across λ in resting and motor task states. **c**–**d**, Estimated EC at $\lambda = 0.7$ in resting state (**c**) and motor task state (**d**): left, mean whole-brain EC matrix; right, seed-to-whole-brain EC maps (white dot: seed) shown for a somatomotor seed (upper right) and a dorsal attention seed (lower right), illustrating state-dependent differences in connectivity patterns. **e**, Higher communication cost in motor task state than resting state across λ ($P = 3.9 \times 10^{-18}$ at $\lambda = 0.7$). **f**, Higher functional efficiency in motor task state than resting state across λ ($P = 8.2 \times 10^{-17}$ at $\lambda = 0.7$). **g**, Higher between-network cost ($P = 3.9 \times 10^{-18}$; left) and efficiency ($P = 5.4 \times 10^{-18}$; right) in motor task state than resting state at $\lambda = 0.7$. **h**–**j**, Task-evoked repositioning along the cost–efficiency trade-off spectrum, shifting brain networks toward a regime with higher efficiency and higher cost during motor (**h**), language (**i**) and working-memory (**j**) task states. P values were obtained using two-sided Wilcoxon signed-rank test, $n = 100$. ***, $P < 0.001$.

cost at $\lambda = 0.7$, two-sided Wilcoxon signed-rank test; Fig. 5e–f). Decomposing these shifts, we found that motor tasks increased between-network efficiency and cost, with a slight decrease in within-network efficiency and cost (Fig. 5g;

Supplementary Fig. 12). This pattern suggests a task-induced move in the tradeoff spectrum toward more integrative between-network communications.

An additional observation is that the motor-task operating point lies largely on, but slightly below, the cost–efficiency trade-off spectrum from the resting state (Fig. 5h), indicating that task states draw on an intrinsic cost–efficiency framework already present at rest, rather than forming a separate configuration. This pattern held across tasks: both language and working-memory tasks exhibited similar shifts along the cost–efficiency spectrum toward higher efficiency and higher cost relative to rest (Fig. 5i–j). Complementary graph metrics revealed reduced modular segregation and local efficiency during tasks, consistent with a shift toward more globally integrative communication (Supplementary Fig. 12). Together, these results demonstrate that cognitive tasks consistently reposition the brain's operating point along the cost–efficiency spectrum, toward a regime of higher functional efficiency accompanied by higher communication cost.

2.5 Task-evoked alterations in cost–efficiency trade-off of the depressive brain

Having established that task engagement repositions whole-brain networks along the cost–efficiency spectrum in healthy participants (Fig. 5), we next examined whether psychiatric disorders disrupt this task-evoked reconfiguration. Specifically, we hypothesized that if disease-related constraints primarily affect the ability to reconfigure brain networks under cognitive demands, group differences would be modest at rest but more pronounced during task engagement [30, 31].

To test this hypothesis, we compared resting state EC with EC during a cognitively demanding task (i.e., promismatch task state) in major depressive disorder (MDD) (Fig. 6a). At $\lambda = 0.7$, group-averaged EC showed little separation between healthy controls (HCs) and MDDs at rest. Both the mean whole-brain EC matrices and the seed-to-whole-brain views anchored in the frontoparietal network (FPN) appeared broadly comparable across groups (Fig. 6b). However, during the promismatch task, group differences became more evident in the same FPN-seeded view (Fig. 6c). HCs showed clearer task-related enhancements in specific couplings, while MDDs displayed EC patterns more similar to their resting-state configuration. Example edges that diverged between groups (solid and dashed circles) illustrate this difference, suggesting reduced task-related EC reconfiguration in MDD.

To explore whether these connection-level differences reflect broader functional changes, we assessed global, within-network, and between-network efficiency at rest and during the task in both HC and MDD groups. At rest, there were no significant group differences ($P = 0.452$, 0.510, and 0.382 for global, within-network and between-network efficiency, two-sided Mann–Whitney U test; Fig. 6d). Remarkably, during the task, significant group differences emerged ($P = 0.040$, 0.722, and 0.040 for global, within-network and between-network efficiency, two-sided Mann–Whitney U test; Fig. 6e).

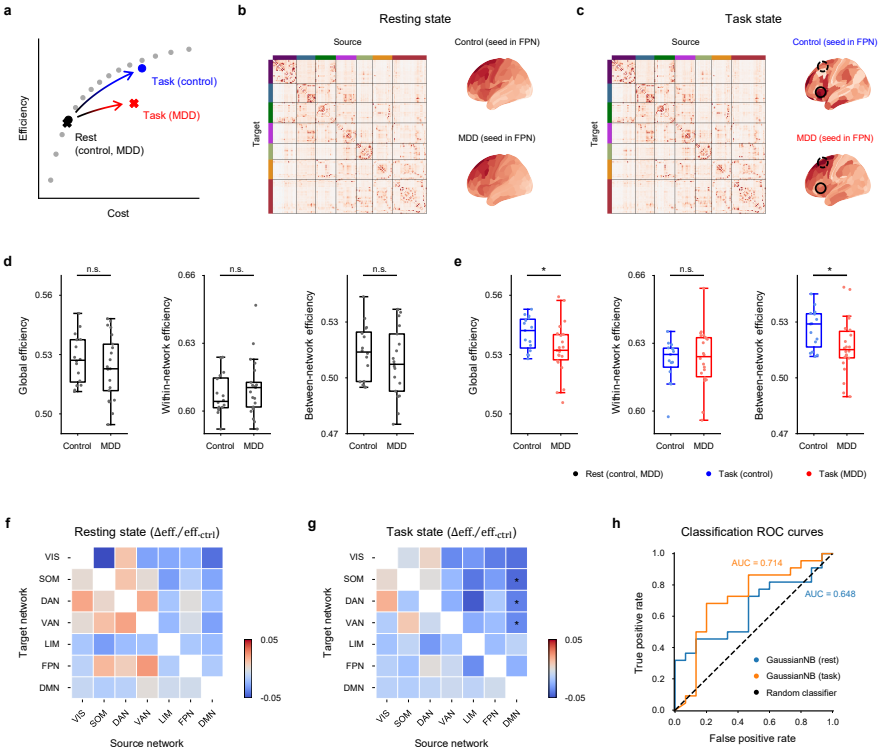

Fig. 6 Task-evoked alterations in cost–efficiency trade-off of the depressive brain. a, Schematic of state-dependent group separation in the cost–efficiency space: control and MDD overlap at rest but diverge during task. **b**–**c**, Group-averaged EC at $\lambda = 0.7$ in resting state (**b**) and promismatch task state (**c**): left, mean whole-brain EC matrix; right, seed-to-whole-brain EC maps from an FPN seed (upper right, control; lower right, MDD). Circles highlight connections stronger in control but weaker in MDD (solid) and weaker in control but stronger in MDD (dashed). **d**–**e**, Group differences (control vs. MDD) in global efficiency, within-network efficiency, and between-network efficiency during resting state ($P = 0.452$, 0.510, 0.382, respectively; **d**) and promismatch task state ($P = 0.040$, 0.722, 0.040, respectively; **e**). **f**–**g**, Network-to-network efficiency change ratios (MDD relative to control) during resting state (**f**) and promismatch task state (**g**). No network-pair differences survived BH-FDR correction in resting state, whereas in promismatch task state, three network-to-network pairs showed BH-FDR-adjusted significance (DMN→SOM, DMN→DAN, and DMN→VAN; $P_{adj} = 0.048$). **h**, ROC curves for classifying control vs. MDD using network-to-network efficiency features, with higher classification performance in the promismatch task state than resting state. P values in **d**–**g** were obtained using two-sided Mann–Whitney U test. P_{adj} values in **f**–**g** were adjusted using Benjamini–Hochberg false discovery rate (BH-FDR) procedure across all network-pair comparisons within each panel. Sample sizes: resting state, $n = 16$ (control) and $n = 21$ (MDD); promismatch task state, $n = 15$ (control) and $n = 22$ (MDD). n.s., not significant; *, $P < 0.05$ in **d**–**e** and $P_{adj} < 0.05$ in **f**–**g**. VIS, visual network; SOM, somatomotor network; DAN, dorsal attention network; VAN, ventral attention network; LIM, limbic network; FPN, frontoparietal network; DMN, default mode network. ROC, receiver operating characteristic; AUC, area under the ROC curve.

These results confirm our hypothesis that task engagement facilitated differences in large-scale communication capacity between HCs and MDDs.

These findings were corroborated by a cross-dataset comparison with a larger resting-state autism dataset (ABIDE, TR = 2 s subset, $n = 242$ controls and $n = 193$ autism), which also showed limited separation in the cost–efficiency landscape between autism participants and healthy controls (Supplementary Fig. 13). These results suggest that resting-state cost–efficiency profiles may be insufficient for distinguishing clinical groups, highlighting the importance of task-state networks for detecting disorder-related deviations.

At the network-to-network level, efficiency change ratios showed no robust differences at rest (Fig. 6f), but during the task, several network-level communications were significantly weakened in MDDs compared to HCs ($P_{\mathrm{adj}} < 0.05$ for DMN→SOM, DMN→DAN, and DMN→VAN; Fig. 6g), indicating task-evoked deficits in inter-network interactions in MDD under cognitive demand. Finally, we tested whether task-evoked alterations could improve the classification of MDDs from HCs. Using network-to-network efficiency features, classification performance was higher during the promismatch task than at rest (AUC = 0.714 for the task state vs. AUC = 0.648 for resting state; Fig. 6h), suggesting that cognitive engagement provides more sensitive features for distinguishing clinical alterations than resting-state alone. Together, these results demonstrate that MDD is associated with disrupted task-evoked reconfiguration along the cost–efficiency spectrum, with task states offering a more sensitive window for detecting psychiatric disease-related changes.

3 Discussion

Human cognitive function relies on coordinated communication among distributed brain networks, yet such communication is constrained by physical distance and energetic limits, requiring a balance between economical wiring and the strategic placement of long-range connections for global integration [32–35]. Our central insight is that the cost–efficiency trade-off should be viewed not as discrete empirical configurations, but as a structured spectrum. This spectrum provides a latent scaffold, enabling navigation across brain states, and allows for comparisons between cognitive states and psychiatric conditions, both in terms of their position on the spectrum and their shifts under cognitive demand. To uncover the latent spectrum, we introduced an explainable linear dynamical model with a tunable spatial distance prior. Previous cost–efficiency studies treat a single observed connectome as a post hoc object for summarizing the brain network properties [23, 36–38]; however, they offer limited insight into how communication architectures might change as constraints vary. Instead, by using spatial embedding as an explicit control parameter, we expose a continuous spectrum of possible interaction architectures anchored to observed brain dynamics, allowing us to make counterfactual comparisons of state shifts and group differences.

The choice of inter-regional distance as the regularizing prior, rather than SC, is crucial for our aims. While SC-informed priors have been used to improve or regularize EC estimation [39–41], it is likely that SC itself is the

product of developmental and multi-objective selection [42, 43]. Using SC as the regularizing prior risks blurring the distinction between the physical constraint we impose and the empirical outcome shaped by that constraint. Consistent with this view, our results show that stronger distance regularization aligns EC more closely with SC (Fig. 2c–d), reinforcing the idea that SC reflects organization shaped by a spatial distance prior.

Within this spectrum, resting-state and task engagement can be interpreted as a baseline operating point with low cost and a demand-evoked shift to a higher-efficiency, higher-cost regime (Fig. 5) [44–46]. In our results, resting-state EC shows lower efficiency at lower cost, consistent with an economical default regime that preserves energy for future cognitive integration [14]. In contrast, task engagement recruits additional integrative interactions at higher cost (Fig. 5e–f), reflecting a functional shift in the brain's operating point. This dynamic rest-to-task reconfiguration allows the brain to flexibly increase integration when needed. Importantly, task-state operating points remain largely on the resting-state-derived spectrum (Fig. 5h–j), suggesting that tasks selectively reweight interactions that are already feasible at rest, rather than forming completely new architectures outside the intrinsic scaffold [47].

This trade-off spectrum is particularly relevant for psychiatry, where group differences are most pronounced under conditions of cognitive demand [48, 49]. Task states act as functional probes of brain dynamics under cognitive pressure [50, 51], which is in line with our evidence from MDD that cognitive challenges under task elicit clinically significant network-level abnormalities, indicating impaired task-evoked reconfiguration (Fig. 6). Specifically, MDD is characterized by impaired long-range integrative coupling, as evidenced by attenuated task-evoked shifts in between-network efficiency (Fig. 6e). This contrasts with the healthy brain, where task engagement promotes a strategic shift toward a higher-efficiency, higher-cost regime (Fig. 5h–j). Within this framework, psychiatric disorders can be characterized by two key features: their operating points and their ability to navigate the cost–efficiency landscape. Our framework moves beyond static measures, offering a dual-dimensional quantification of brain network function that encompasses both baseline operation and reconfigurability. This approach shows promise for linking network dynamics to clinical symptoms and assessing interventions aimed at restoring cognitive flexibility.

We highlight two extensions to broaden this framework. First, although the GA-derived Pareto front provides a useful reference boundary, the gap between empirical EC and the front suggest the potential for additional optimization objectives beyond cost and efficiency. Future work could expand the set of objectives (such as robustness, flexibility, and topological complexity) and benchmark EC against these fronts to explore the principles governing real brain organization [52–54]. Second, while task-state operating points align with the resting-state-derived spectrum, we observe task-specific deviations that may reflect transient, context-dependent interactions not consolidated at rest. These may be associated with skill acquisition, automaticity, or task

performance [55, 56]. Future studies linking these deviations to behavioral measures would test whether both spectrum position and off-spectrum displacement can provide insight into cognitive efficiency and learning-related reconfiguration.

4 Methods

4.1 Data processing

We analyzed fMRI data from HCP [57], CHCP [58], and an OpenNeuro major depressive disorder dataset (ds006731, v1.0.0) [59]. Analyses used a subset of 100 healthy adults per cohort for HCP and CHCP. For HCP, we analyzed resting-state fMRI and three task paradigms (motor, language, working memory); the repetition time was 0.72 s. For CHCP, we analyzed resting-state fMRI; the repetition time was 0.71 s. For ds006731, we included all available data from the rest and Promismatch conditions, comprising rest scans from 16 healthy controls and 21 participants with MDD, and Promismatch scans from 15 healthy controls and 22 participants with MDD; the repetition time was 3.00 s.

For HCP and CHCP, images were processed with the HCP Minimal Preprocessing Pipeline [60] to produce standardized volumes and cortical surfaces in a common space. Briefly, preprocessing included motion correction, EPI distortion correction, coregistration of fMRI to each participant's T1-weighted anatomy, and normalization to the MNI152 standard space. For ds006731, we preprocessed the data with fMRIPrep [61], normalized the outputs to the MNI152 standard space, and discarded the first 10 TRs of each run before subsequent analyses.

Parcel-wise BOLD signals were extracted using Nilearn with the MMP1.0 cortical parcellation (360 parcels; 180 per hemisphere) [62]. For each run, we linearly detrended the BOLD signals, applied a 0.01–0.10 Hz band-pass filter to focus on low-frequency fluctuations commonly analyzed in fMRI connectivity, and z-scored each parcel. Following Luo et al. [25], parcels were assigned to seven networks defined by Yeo et al. [63], comprising visual (VIS), somatomotor (SOM), dorsal attention (DAN), ventral attention (VAN), limbic (LIM), frontoparietal control (FPN), and default mode (DMN).

When studying the relationship between EC and SC, we used the group-average SC provided by Demirtaş et al. [64], derived from diffusion MRI using FSL's bedpostx and probtrackx2 probabilistic tractography workflows. The SC matrix was scaled to [0,1], and log-transformed. For an external EC reference, we used the publicly available group-average NPI-EC [25]. To assess whether our EC estimates capture plausible inter-individual differences, we additionally ran NPI for each participant to obtain individual-level NPI-EC matrices and compared the resulting NPI-EC with our EC.

4.2 Distance-constrained linear dynamical model

4.2.1 Model specification

Let $\boldsymbol{x}_t \in \mathbb{R}^N$ denote the parcel-wise BOLD vector at time t, where N is the number of cortical parcels ($N = 360$ for MMP1.0). We model single-step dynamics with a linear map

$$\boldsymbol{x}_{t+1} = \boldsymbol{W}\boldsymbol{x}_t + \boldsymbol{\varepsilon}_t, \;\; \boldsymbol{\varepsilon}_t \sim \mathcal{N}(0, \sigma^2\mathbf{I}). \tag{1}$$

Here $\boldsymbol{\varepsilon}_t$ denotes i.i.d. additive Gaussian noise with covariance $\sigma^2\mathbf{I}$. The EC matrix $\boldsymbol{W} \in \mathbb{R}^{N\times N}$ is directed and signed: entry W_{ij} quantifies the influence of source parcel j at time t on target parcel i at time $t+1$. Thus, row i collects inputs into region i, and column j collects outputs from region j. Parcel BOLD signals are z-scored, so we do not include an intercept term in the model.

4.2.2 Spatial distance regularization

To encode a spatial prior, we estimate $\boldsymbol{W}$ by minimizing a one-step prediction error augmented with a distance-weighted regularizer. The distance weights are given by a standardized parcel-wise Euclidean distance matrix $\boldsymbol{D}$. Let d_{ij} be the Euclidean distance between the MMP1.0 parcel centroids. We rescale off-diagonal distances so their mean equals 1 and set the diagonal to 1 so that self-couplings W_{ii} receive the same baseline regularization:

$$\bar{d}_{\text{off}} = \frac{1}{N(N-1)}\sum_{i\neq j} d_{ij}, \;\; D_{ij} = \begin{cases} d_{ij}/\bar{d}_{\text{off}}, & i \neq j, \\ 1, & i = j. \end{cases} \tag{2}$$

Using $\boldsymbol{D}$, we estimate $\boldsymbol{W}$ by minimizing the sum of a one-step prediction error and a distance-weighted penalty:

$$\mathcal{L}(\boldsymbol{W}) = (1-\lambda)\frac{1}{T}\sum_{t=1}^{T}\|\boldsymbol{x}_{t+1} - \boldsymbol{W}\boldsymbol{x}_t\|_2^2 + \lambda\Omega\left(\boldsymbol{W};\boldsymbol{D}\right), \;\; \lambda \in [0,1], \tag{3}$$

where T denotes the number of available one-step training samples and λ balances the prediction error and the distance-weighted regularization.

We considered two choices for Ω:

$$\Omega_{\text{ridge}}(\boldsymbol{W};\boldsymbol{D}) = \left\|\boldsymbol{D}^{1/2}\circ\boldsymbol{W}\right\|_F^2 = \sum_{i,j} D_{ij}W_{ij}^2, \tag{4}$$

$$\Omega_{\text{lasso}}(\boldsymbol{W};\boldsymbol{D}) = \|\boldsymbol{D}\circ\boldsymbol{W}\|_1 = \sum_{i,j} D_{ij}|W_{ij}|, \tag{5}$$

where $\circ$ denotes the Hadamard product and $\boldsymbol{D}^{1/2}$ is the element-wise square root. Because D_{ij} increases with inter-parcel distance, long-range interactions are penalized more strongly, encoding a spatial prior.

4.2.3 Parameter estimation

We optimized equation (3) by gradient descent. Updates used all available training samples in a full-batch manner, formed from consecutive pairs $(\boldsymbol{x}_t, \boldsymbol{x}_{t+1})$. We used 80% of the data for training and 20% for evaluation. The held-out evaluation block was contiguous in time to avoid temporal leakage. The implementation was performed in PyTorch on an NVIDIA GeForce RTX 4080 GPU.

For resting state in HCP and CHCP datasets, for each participant and each $\lambda \in \{0.02, 0.04, \ldots, 0.98\}$, we fitted an individual $\boldsymbol{W}$ using the training data. We used a learning rate of 0.01 and trained for 500 epochs. Given the length of the resting-state runs, we did not observe overfitting on the held-out evaluation data (Supplementary Fig. 14, Supplementary Fig. 15).

For task state in HCP dataset, per-participant data are shorter, so we used a two-stage procedure for each task and each $\lambda \in \{0.02, 0.04, \ldots, 0.98\}$. First, we performed population initialization by pooling the data across participants within the same task, and trained with a learning rate of 0.01 for 1000 epochs to obtain $\boldsymbol{W}^{\text{init}}_{\text{task},\lambda}$. Second, we conducted subject-specific fine-tuning: for each task and λ, we selected the number of fine-tuning epochs $k \in \{5, 10, \ldots, 50\}$ that maximized the participant-averaged held-out R^2 on the evaluation data when fine-tuning at a learning rate of 0.001. Each participant's task EC was then obtained by initializing at $\boldsymbol{W}^{\text{init}}_{\text{task},\lambda}$ and fine-tuning for k epochs at a learning rate of 0.001.

For the ds006731 dataset, data length is also short for both rest and task conditions. We therefore adopted the same two-stage procedure as for task data: for each λ, we first obtained a global initialization $\mathbf{W}^{\text{init}}_{\lambda}$ by pooling data across all conditions and diagnostic groups. We then performed subject-specific fine-tuning, selecting the number of fine-tuning epochs $k \in \{5, 10, \ldots, 50\}$ based on held-out R^2; for computational efficiency, the k selection was performed by randomly subsampling 100 runs for fine-tuning when evaluating candidate k values. Each participant's EC for each condition was then obtained by initializing at $\boldsymbol{W}^{\text{init}}_{\lambda}$ and fine-tuning for k epochs.

4.3 Model evaluation

4.3.1 Predictive accuracy on held-out data

To quantify one–step predictive performance, we computed the coefficient of determination R^2 on held-out data, parcel by parcel, and then averaged across parcels. For parcel i with empirical signal $\{y_{i,t}\}_{t\in\mathcal{S}}$ and model prediction $\{\hat{y}_{i,t}\}_{t\in\mathcal{S}}$ on the evaluation split $\mathcal{S}$,

$$R^2_i = 1 - \frac{\sum_{t\in\mathcal{S}} \left(y_{i,t} - \hat{y}_{i,t}\right)^2}{\sum_{t\in\mathcal{S}} \left(y_{i,t} - \bar{y}_i\right)^2}, \quad \bar{y}_i = \frac{1}{|\mathcal{S}|} \sum_{t\in\mathcal{S}} y_{i,t}. \tag{6}$$

The overall metric is the mean over parcels. We used five-fold blocked cross-validation: in each fold, a contiguous 20% segment in time served as the evaluation block and the remaining 80% as training, ensuring no temporal leakage. Reported performance is the average of the overall metric across the five folds.

4.3.2 Alignment of EC with SC

For each λ, we first averaged the estimated EC matrices across participants to obtain a group EC matrix. To assess anatomical alignment, we then computed the Pearson correlation between the off-diagonal entries of the group EC and those of the log-transformed SC.

4.3.3 Model-empirical FC correspondence

Given an estimated EC, we generated a long synthetic BOLD signal (length $T_{\text{sim}} = 10000$ in our analyses) by driving the linear dynamics with i.i.d. Gaussian noise $\boldsymbol{\eta}_t$,

$$\boldsymbol{x}_{t+1} = \boldsymbol{W}\boldsymbol{x}_t + \boldsymbol{\eta}_t, \;\; \boldsymbol{\eta}_t \sim \mathcal{N}\left(\mathbf{0},\, \sigma^2\mathbf{I}\right), \tag{7}$$

where $\boldsymbol{W}$ is the estimated EC, $\sigma = 0.1$ in our analyses, and the initial condition was $\boldsymbol{x}_0 = \mathbf{0} \in \mathbb{R}^N$. From the simulated series we computed the model FC as the parcel-parcel Pearson correlation matrix. The empirical FC was computed from the data used to estimate $\boldsymbol{W}$. Correspondence was quantified as the Pearson correlation between vectorized off-diagonal entries of the model FC and those of the empirical FC.

4.3.4 Alignment with NPI-EC

For each λ, we first averaged the estimated EC matrices across participants to obtain a group EC matrix. Alignment with NPI-EC was quantified as the Pearson correlation between the off-diagonal entries of the estimated EC and those of the publicly available group-average NPI-EC. In Luo et al. [25], NPI-EC$_{ij}$ represents a directed connection from region i to region j, whereas in our convention W_{ij} encodes the influence from region j to region i; thus we transposed NPI-EC before computing the correlation.

4.4 Graph-theoretic metrics

Graph metrics were computed on a binary directed adjacency matrix derived from EC. For each participant and each λ, we ranked the off-diagonal entries of $|\boldsymbol{W}|$ and set the top 15% to 1, with all other off-diagonal entries and the diagonal set to 0. Denote the resulting adjacency matrix by $\boldsymbol{A} \in \{0,1\}^{N\times N}$.

4.4.1 Global communication cost

Let $D \in \mathbb{R}_{+}^{N\times N}$ be the parcel-wise distance matrix defined in equation (2). Global cost normalizes the distance-weighted edge load to $[0,1]$:

$$C\left(\boldsymbol{W}\right) \coloneqq C\left(\boldsymbol{A}\right) = \frac{\sum_{i\neq j} A_{ij} D_{ij}}{\sum_{i\neq j} D_{ij}} \in [0,1]\,. \tag{8}$$

Thus, a graph with no inter-areal edges has $C\left(\boldsymbol{A}\right) = 0$, while a complete directed graph has $C\left(\boldsymbol{A}\right) = 1$.

4.4.2 Global functional efficiency

On the binary directed graph $\boldsymbol{A}$ we computed shortest paths between all ordered node pairs. Let ℓ_{ij} be the minimal number of directed steps from node j to node i; if i is unreachable from j then $\ell_{ij} = +\infty$. ℓ_{ij} was computed on $\boldsymbol{A}$ using the Brain Connectivity Toolbox [65]. Global efficiency is the mean reciprocal path length over ordered pairs,

$$E\left(\boldsymbol{W}\right) \coloneqq E\left(\boldsymbol{A}\right) = \frac{1}{N\left(N-1\right)} \sum_{i\neq j} \frac{1}{\ell_{ij}}, \quad \frac{1}{+\infty} \coloneqq 0. \tag{9}$$

Global efficiency lies in $[0,1]$: it equals 0 for an empty graph and 1 for a complete directed graph.

4.4.3 Within- and between-network cost

Let $g(i) \in \{1,\ldots,7\}$ denote the Yeo7 network assignment of parcel i. Define the within-network and between-network masks as

$$M_{ij}^{\text{within}} = \begin{cases} 1, & i \neq j,\ \ g(i) = g(j), \\ 0, & \text{otherwise}, \end{cases} \tag{10}$$

$$M_{ij}^{\text{between}} = \begin{cases} 1, & g(i) \neq g(j), \\ 0, & \text{otherwise}. \end{cases} \tag{11}$$

Within- and between-network costs quantify the distance-weighted loads restricted to the corresponding masks. Intuitively, $C(\boldsymbol{W})_{\text{within}}$ captures the communication burden carried by connections confined within the same Yeo7 network, whereas $C(\mathbf{W})_{\text{between}}$ captures the burden carried by cross-network links. Both costs are normalized to $[0,1]$:

$$C(\boldsymbol{W})_{\text{within}} \coloneqq C(\boldsymbol{A})_{\text{within}} = \frac{\sum_{i\neq j} A_{ij} D_{ij} M_{ij}^{\text{within}}}{\sum_{i\neq j} D_{ij} M_{ij}^{\text{within}}}, \tag{12}$$

$$C(\boldsymbol{W})_{\text{between}} \coloneqq C(\boldsymbol{A})_{\text{between}} = \frac{\sum_{i\neq j} A_{ij} D_{ij} M_{ij}^{\text{between}}}{\sum_{i\neq j} D_{ij} M_{ij}^{\text{between}}}. \tag{13}$$

4.4.4 Within- and between-network efficiency

Define the index sets $\mathcal{P}_{\text{within}} = \{(i,j) : i \neq j,\ M_{ij}^{\text{within}} = 1\}$ and $\mathcal{P}_{\text{between}} = \{(i,j) : i \neq j,\ M_{ij}^{\text{between}} = 1\}$. Within- and between-network efficiency average the reciprocals of shortest-path lengths over the corresponding index sets:

$$E\left(\boldsymbol{W}\right)_{\text{within}} \coloneqq E\left(\boldsymbol{A}\right)_{\text{within}} = \frac{1}{|\mathcal{P}_{\text{within}}|} \sum_{(i,j)\in\mathcal{P}_{\text{within}}} \frac{1}{\ell_{ij}}, \tag{14}$$

$$E\left(\boldsymbol{W}\right)_{\text{between}} \coloneqq E\left(\boldsymbol{A}\right)_{\text{between}} = \frac{1}{|\mathcal{P}_{\text{between}}|} \sum_{(i,j)\in\mathcal{P}_{\text{between}}} \frac{1}{\ell_{ij}}. \tag{15}$$

Intuitively, $E(\boldsymbol{W})_{\text{within}}$ is high when nodes sharing the same Yeo7 label can reach each other through relatively few steps, while $E(\boldsymbol{W})_{\text{between}}$ is high when nodes from different labels are connected through short routes.

4.4.5 Network-to-network cost

Let $g(i) \in \{1, \ldots, 7\}$ denote the Yeo7 network assignment of parcel i. For any ordered pair of networks (p, q) (allowing $p = q$), define the directed mask

$$M_{ij}^{p\to q} = \begin{cases} 1, & i \neq j,\ \ g(j) = p,\ \ g(i) = q, \\ 0, & \text{otherwise.} \end{cases} \tag{16}$$

The directed network-to-network cost from p to q summarizes the distance-weighted load specifically carried by edges from network p to network q, and is normalized to $[0, 1]$:

$$C(\boldsymbol{W})_{p\to q} \coloneqq C(\boldsymbol{A})_{p\to q} = \frac{\sum_{i\neq j} A_{ij} D_{ij} M_{ij}^{p\to q}}{\sum_{i\neq j} D_{ij} M_{ij}^{p\to q}}. \tag{17}$$

4.4.6 Network-to-network efficiency

Define the index set $\mathcal{P}_{p\to q} = \{(i,j) : i \neq j,\ M_{ij}^{p\to q} = 1\}$. The directed network-to-network efficiency from p to q summarizes how efficiently information can travel from network p to network q by averaging the reciprocals of shortest-path lengths:

$$E(\boldsymbol{W})_{p\to q} \coloneqq E(\boldsymbol{A})_{p\to q} = \frac{1}{|\mathcal{P}_{p\to q}|} \sum_{(i,j)\in\mathcal{P}_{p\to q}} \frac{1}{\ell_{ij}}. \tag{18}$$

4.4.7 Robustness to edge removal

We quantified robustness by targeted removal of high–betweenness edges on the binary directed graph $\boldsymbol{A}$. For a present edge e, its edge betweenness

centrality is

$$\mathrm{bc}(e) = \sum_{u \neq v} \frac{\sigma_{uv}(e)}{\sigma_{uv}}, \tag{19}$$

where σ_{uv} denotes the number of directed shortest paths from node v to node u in $\boldsymbol{A}$, and $\sigma_{uv}(e)$ counts those paths that traverse e; ordered pairs with $\sigma_{uv} = 0$ are omitted from the sum.

For each participant and each λ, we ranked present edges by $\mathrm{bc}(e)$ and removed the top fraction $f \in \{0.05, 0.10, \ldots, 0.60\}$. Let τ_f be the largest threshold such that at least a fraction f of edges in $\boldsymbol{A}$ satisfy $\mathrm{bc}(e) \geq \tau_f$, and let $\mathcal{R}_f = \{e : \mathrm{bc}(e) \geq \tau_f\}$ be the removed set. The post-attack adjacency matrix is

$$(A_f)_{ij} = A_{ij} \mathbf{1}\left[(j \to i) \notin \mathcal{R}_f\right]. \tag{20}$$

Global efficiency was computed using equation (9). Robustness was summarized by the relative efficiency,

$$\rho(f) = \frac{E(\boldsymbol{A}_f)}{E(\boldsymbol{A})}, \tag{21}$$

with smaller $\rho(f)$ indicating greater vulnerability under targeted edge removal.

4.5 Pareto-front construction and related metrics

4.5.1 Multi-objective genetic algorithm for the Pareto front $\mathcal{P}$

We searched over binary directed adjacencies at fixed density (15% of off-diagonal entries set to 1) using a multi-objective genetic algorithm [66]. Each candidate was encoded as a length-$N(N-1)$ bit string (diagonal fixed at 0); crossover and mutation were followed by a repair step to maintain the density constraint. The two objectives were to minimize the global communication cost $C(\boldsymbol{A})$ defined in equation (8) and to maximize the global functional efficiency $E(\boldsymbol{A})$ defined in equation (9). Non-dominated solutions obtained during evolution formed an empirical Pareto set $\mathcal{P}$ that approximates the cost–efficiency trade-off front.

4.5.2 Optimization degree

Let $c_{\min} = \min_{\boldsymbol{B} \in \mathcal{P}} C(\boldsymbol{B})$ and $e_{\max} = \max_{\boldsymbol{B} \in \mathcal{P}} E(\boldsymbol{B})$ denote, respectively, the smallest cost and largest efficiency observed on the Pareto front. For normalization we also defined $c_{\max}$ and $e_{\min}$ as the maximal cost and minimal efficiency attainable within the feasible set under the same density constraint. For any adjacency matrix $\boldsymbol{A}$ derived from $\boldsymbol{W}$, the optimization degree is

$$\mathrm{optdeg}\,(\boldsymbol{A}) = \frac{1}{2}\left[\frac{E(\boldsymbol{A}) - e_{\min}}{e_{\max} - e_{\min}} + \frac{c_{\max} - C(\boldsymbol{A})}{c_{\max} - c_{\min}}\right] \in [0, 1], \tag{22}$$

which treats cost and efficiency as equally important (Supplementary Fig. 16); higher values indicate better cost–efficiency balance.

4.5.3 Matched comparators

Let $\boldsymbol{A}^{(p)}$ denote the binarized EC adjacency of participant p. Define $\overline{C}$ and $\overline{E}$ as the across-participant means of global communication cost $C(\boldsymbol{A}^{(p)})$ and functional efficiency $E(\boldsymbol{A}^{(p)})$ respectively. We then selected three Pareto comparators from $\mathcal{P}$:

$$\boldsymbol{B}_{\text{cost}} = \arg\min_{\boldsymbol{B}\in\mathcal{P}} \left|C(\boldsymbol{B}) - \overline{C}\right| \quad \text{(cost-matched Pareto)}, \tag{23}$$

$$\boldsymbol{B}_{\text{eff}} = \arg\min_{\boldsymbol{B}\in\mathcal{P}} \left|E(\boldsymbol{B}) - \overline{E}\right| \quad \text{(efficiency-matched Pareto)}, \tag{24}$$

$$\boldsymbol{B}_{\text{opt}} = \arg\max_{\boldsymbol{B}\in\mathcal{P}} \ \text{optdeg}(\boldsymbol{B}) \quad \text{(optimal Pareto)}. \tag{25}$$

4.5.4 Similarity between EC and Pareto solutions

For each participant and each λ of interest, let $\boldsymbol{A}$ be the binarized EC adjacency matrix and let $\boldsymbol{P} \in \{\boldsymbol{B}_{\text{cost}}, \boldsymbol{B}_{\text{eff}}, \boldsymbol{B}_{\text{opt}}\}$ be a selected Pareto comparator. Denote the sets of present directed edges by $\mathcal{E}(\boldsymbol{A}) = \{(i,j) : i \neq j,\ A_{ij} = 1\}$ and $\mathcal{E}(\boldsymbol{P})$. We quantified similarity with the Dice coefficient:

$$\text{Dice}(\boldsymbol{A}, \boldsymbol{P}) = \frac{2\,|\mathcal{E}(\boldsymbol{A}) \cap \mathcal{E}(\boldsymbol{P})|}{|\mathcal{E}(\boldsymbol{A})| + |\mathcal{E}(\boldsymbol{P})|} \in [0,1], \tag{26}$$

which is insensitive to the large number of absent edges in sparse graphs.

4.6 Disease classification using network-to-network efficiency features

Binary classification was used to distinguish healthy controls from participants with MDD based on large-scale communication features derived from EC. For each participant and each state (rest and promismatch), a feature vector was constructed from directed network-to-network efficiency values between Yeo7 networks computed from the binarized EC matrix at $\lambda = 0.7$. All directed inter-network pairs were included while excluding within-network entries, yielding a fixed-dimensional feature vector per participant. No additional feature scaling or transformation was applied.

A Gaussian Naive Bayes classifier was evaluated using stratified 10-fold cross-validation repeated 500 times with fold shuffling to obtain stable performance estimates in this modest-sample setting. In each repetition, out-of-fold predicted probabilities were obtained for every participant. For visualization and summary, out-of-fold predicted probabilities were averaged across the 500 repetitions to obtain a single predicted probability per participant. ROC curves were computed by sweeping a threshold over these averaged predicted probabilities and comparing the resulting labels to the ground-truth group labels. AUC was computed from the same ROC curves.

Declarations

All the authors declare no conflict of interest.

Data availability

Datasets used in this study are accessible via their respective repositories: HCP dataset (https://www.humanconnectome.org/study/hcp-young-adult/document/1200-subjects-data-release), CHCP dataset (https://cstr.cn/31253.11.sciencedb.01374), MDD dataset (https://openneuro.org/datasets/ds006731/versions/1.0.0). The brain atlases used in this study are also publicly available: MMP atlas (https://github.com/mbedini/The-HCP-MMP1.0-atlas-in-FSL), Schaefer atlases (https://github.com/ThomasYeoLab/CBIG/tree/master/stable_projects/brain_parcellation/Schaefer2018_LocalGlobal/Parcellations/MNI).

Code availability

The code supporting this study is available on GitHub at https://github.com/ncclab-sustech/Dynamic-Cost-Efficiency-Tradeoff, under the Apache License, v.2.0 (Apache-2.0).

Acknowledgements

The authors would like to thank Dr. Ziwei Dai and Dr. Zhichao Liang from the Southern University of Science and Technology for their valuable suggestions. This work was supported by the National Natural Science Foundation of China (62472206, 325B2044), National Key R&D Program of China (2025YFC3410000), Shenzhen Science and Technology Innovation Committee (RCYX20231211090405003, JCYJ20220818100213029), Guangdong Provincial Key Laboratory of Advanced Biomaterials (2022B1212010003), and the open research fund of the Guangdong Provincial Key Laboratory of Mathematical and Neural Dynamical Systems, the Center for Computational Science and Engineering at Southern University of Science and Technology.

References

[1] Avena-Koenigsberger, A., Misic, B. & Sporns, O. Communication dynamics in complex brain networks. *Nature reviews neuroscience* **19**, 17–33 (2018).

[2] Seguin, C., Sporns, O. & Zalesky, A. Brain network communication: concepts, models and applications. *Nature reviews neuroscience* **24**, 557–574 (2023).

[3] Akarca, D., Vértes, P. E., Bullmore, E. T. & Astle, D. E. A generative network model of neurodevelopmental diversity in structural brain organization. *Nature communications* **12**, 4216 (2021).

[4] Achterberg, J., Akarca, D., Strouse, D., Duncan, J. & Astle, D. E. Spatially embedded recurrent neural networks reveal widespread links between structural and functional neuroscience findings. *Nature Machine Intelligence* **5**, 1369–1381 (2023).

[5] Bressler, S. L. & Menon, V. Large-scale brain networks in cognition: emerging methods and principles. *Trends in cognitive sciences* **14**, 277–290 (2010).

[6] Bassett, D. S. & Sporns, O. Network neuroscience. *Nature neuroscience* **20**, 353–364 (2017).

[7] Gustafsson, J., Robinson, J. L., Zetterberg, H. & Nielsen, J. Brain energy metabolism is optimized to minimize the cost of enzyme synthesis and transport. *Proceedings of the National Academy of Sciences* **121**, e2305035121 (2024).

[8] Deng, S., Li, J., Thomas Yeo, B. & Gu, S. Control theory illustrates the energy efficiency in the dynamic reconfiguration of functional connectivity. *Communications biology* **5**, 295 (2022).

[9] Liang, X. *et al.* Dissecting human cortical similarity networks across the lifespan. *Neuron* **113**, 3275–3295 (2025).

[10] Finc, K. *et al.* Dynamic reconfiguration of functional brain networks during working memory training. *Nature communications* **11**, 2435 (2020).

[11] Luppi, A. I. *et al.* Contributions of network structure, chemoarchitecture and diagnostic categories to transitions between cognitive topographies. *Nature Biomedical Engineering* **8**, 1142–1161 (2024).

[12] Goulas, A., Betzel, R. F. & Hilgetag, C. C. Spatiotemporal ontogeny of brain wiring. *Science advances* **5**, eaav9694 (2019).

[13] Park, H.-J. & Friston, K. Structural and functional brain networks: from connections to cognition. *Science* **342**, 1238411 (2013).

[14] Bullmore, E. & Sporns, O. The economy of brain network organization. *Nature reviews neuroscience* **13**, 336–349 (2012).

[15] Friston, K. J. Functional and effective connectivity in neuroimaging: a synthesis. *Human brain mapping* **2**, 56–78 (1994).

[16] Salvador, R. *et al.* Neurophysiological architecture of functional magnetic resonance images of human brain. *Cerebral cortex* **15**, 1332–1342 (2005).

[17] Meunier, D., Lambiotte, R., Fornito, A., Ersche, K. & Bullmore, E. T. Hierarchical modularity in human brain functional networks. *Frontiers in neuroinformatics* **3**, 571 (2009).

[18] Bullmore, E. & Sporns, O. Complex brain networks: graph theoretical analysis of structural and functional systems. *Nature reviews neuroscience* **10**, 186–198 (2009).

[19] Rubinov, M. & Sporns, O. Complex network measures of brain connectivity: uses and interpretations. *Neuroimage* **52**, 1059–1069 (2010).

[20] Sun, L. *et al.* Human lifespan changes in the brain's functional connectome. *Nature neuroscience* 1–11 (2025).

[21] Li, J. *et al.* A thresholding method based on society modularity and role division for functional connectivity analysis. *Journal of Neural Engineering* **19**, 056030 (2022).

[22] Luppi, A. I., Rosas, F. E., Mediano, P. A., Menon, D. K. & Stamatakis, E. A. Information decomposition and the informational architecture of the brain. *Trends in Cognitive Sciences* **28**, 352–368 (2024).

[23] Bassett, D. S. *et al.* Cognitive fitness of cost-efficient brain functional networks. *Proceedings of the National Academy of Sciences* **106**, 11747–11752 (2009).

[24] Nozari, E. *et al.* Macroscopic resting-state brain dynamics are best described by linear models. *Nature biomedical engineering* **8**, 68–84 (2024).

[25] Luo, Z. *et al.* Mapping effective connectivity by virtually perturbing a surrogate brain. *Nature Methods* 1–10 (2025).

[26] Perich, M. G. *et al.* Inferring brain-wide interactions using data-constrained recurrent neural network models. *BioRxiv* 2020–12 (2020).

[27] Chen, Y., Rosen, B. Q. & Sejnowski, T. J. Dynamical differential covariance recovers directional network structure in multiscale neural systems. *Proceedings of the National Academy of Sciences* **119**, e2117234119 (2022).

[28] Patow, G., Martin, I., Sanz Perl, Y., Kringelbach, M. L. & Deco, G. Whole-brain modelling: an essential tool for understanding brain dynamics. *Nature Reviews Methods Primers* **4**, 53 (2024).

[29] Ma, L. *et al.* Working memory load modulation of parieto-frontal connections: Evidence from dynamic causal modeling. *Human brain mapping* **33**, 1850–1867 (2012).

[30] Braun, U. *et al.* Dynamic reconfiguration of frontal brain networks during executive cognition in humans. *Proceedings of the National Academy of Sciences* **112**, 11678–11683 (2015).

[31] Kaiser, R. H. *et al.* Dynamic resting-state functional connectivity in major depression. *Neuropsychopharmacology* **41**, 1822–1830 (2016).

[32] Attwell, D. & Laughlin, S. B. An energy budget for signaling in the grey matter of the brain. *Journal of Cerebral Blood Flow & Metabolism* **21**, 1133–1145 (2001).

[33] Chklovskii, D. B., Schikorski, T. & Stevens, C. F. Wiring optimization in cortical circuits. *Neuron* **34**, 341–347 (2002).

[34] Van Den Heuvel, M. P. & Sporns, O. Rich-club organization of the human connectome. *Journal of Neuroscience* **31**, 15775–15786 (2011).

[35] Deco, G. *et al.* Rare long-range cortical connections enhance human information processing. *Current Biology* **31**, 4436–4448 (2021).

[36] Achard, S. & Bullmore, E. Efficiency and cost of economical brain functional networks. *PLoS computational biology* **3**, e17 (2007).

[37] Chen, Y., Wang, S., Hilgetag, C. C. & Zhou, C. Features of spatial and functional segregation and integration of the primate connectome revealed by trade-off between wiring cost and efficiency. *PLoS computational biology* **13**, e1005776 (2017).

[38] Ma, J., Zhang, J., Lin, Y. & Dai, Z. Cost-efficiency trade-offs of the human brain network revealed by a multiobjective evolutionary algorithm. *NeuroImage* **236**, 118040 (2021).

[39] Greaves, M. D., Novelli, L., Mansour L, S., Zalesky, A. & Razi, A. Structurally informed models of directed brain connectivity. *Nature Reviews Neuroscience* **26**, 23–41 (2025).

[40] Stephan, K. E., Tittgemeyer, M., Knösche, T. R., Moran, R. J. & Friston, K. J. Tractography-based priors for dynamic causal models. *Neuroimage* **47**, 1628–1638 (2009).

[41] Crimi, A., Dodero, L., Sambataro, F., Murino, V. & Sona, D. Structurally constrained effective brain connectivity. *NeuroImage* **239**, 118288 (2021).

[42] Ma, J. *et al.* Trade-offs among cost, integration, and segregation in the human connectome. *Network Neuroscience* **7**, 604–631 (2023).

[43] Zhuo, Z. *et al.* Charting brain morphology in international healthy and neurological populations. *Nature Neuroscience* 1–15 (2025).

[44] Cohen, J. R. & D'Esposito, M. The segregation and integration of distinct brain networks and their relationship to cognition. *Journal of Neuroscience* **36**, 12083–12094 (2016).

[45] Shine, J. M. *et al.* The dynamics of functional brain networks: integrated network states during cognitive task performance. *Neuron* **92**, 544–554 (2016).

[46] Luppi, A. I. *et al.* A synergistic core for human brain evolution and cognition. *Nature neuroscience* **25**, 771–782 (2022).

[47] Cole, M. W., Bassett, D. S., Power, J. D., Braver, T. S. & Petersen, S. E. Intrinsic and task-evoked network architectures of the human brain. *Neuron* **83**, 238–251 (2014).

[48] Fang, Z., Lynn, E., Knott, V. J. & Jaworska, N. Functional connectivity profiles in remitted depression and their relation to ruminative thinking. *NeuroImage: Clinical* **45**, 103716 (2025).

[49] Williams, L. M. *et al.* Amygdala reactivity to emotional faces in the prediction of general and medication-specific responses to antidepressant treatment in the randomized ispot-d trial. *Neuropsychopharmacology* **40**, 2398–2408 (2015).

[50] Finn, E. S. Is it time to put rest to rest? *Trends in cognitive sciences* **25**, 1021–1032 (2021).

[51] Zhao, W. *et al.* Task fmri paradigms may capture more behaviorally relevant information than resting-state functional connectivity. *NeuroImage* **270**, 119946 (2023).

[52] Avena-Koenigsberger, A. *et al.* Using pareto optimality to explore the topology and dynamics of the human connectome. *Philosophical Transactions of the Royal Society B: Biological Sciences* **369**, 20130530 (2014).

[53] Pallasdies, F., Norton, P., Schleimer, J.-H. & Schreiber, S. Neural optimization: Understanding trade-offs with pareto theory. *Current opinion in neurobiology* **71**, 84–91 (2021).

[54] Jedlicka, P., Bird, A. D. & Cuntz, H. Pareto optimality, economy–effectiveness trade-offs and ion channel degeneracy: improving population modelling for single neurons. *Open biology* **12**, 220073 (2022).

[55] Bassett, D. S. *et al.* Dynamic reconfiguration of human brain networks during learning. *Proceedings of the National Academy of Sciences* **108**, 7641–7646 (2011).

[56] Hearne, L. J., Cocchi, L., Zalesky, A. & Mattingley, J. B. Reconfiguration of brain network architectures between resting-state and complexity-dependent cognitive reasoning. *Journal of Neuroscience* **37**, 8399–8411 (2017).

[57] Van Essen, D. C. *et al.* The wu-minn human connectome project: an overview. *Neuroimage* **80**, 62–79 (2013).

[58] Yang, G., Ge, J. & Gao, J.-H. Chinese Human Connectome Project (2024). URL https://doi.org/10.11922/sciencedb.01374.

[59] Ekpo, E. *et al.* Resting-state and task-based functional connectivity reveal distinct mpfc and hippocampal network alterations in major depressive disorder. *Brain Sciences* **15**, 1133 (2025).

[60] Glasser, M. F. *et al.* The minimal preprocessing pipelines for the human connectome project. *Neuroimage* **80**, 105–124 (2013).

[61] Esteban, O. *et al.* fmriprep: a robust preprocessing pipeline for functional mri. *Nature methods* **16**, 111–116 (2019).

[62] Glasser, M. F. *et al.* A multi-modal parcellation of human cerebral cortex. *Nature* **536**, 171–178 (2016).

[63] Yeo, B. T. *et al.* The organization of the human cerebral cortex estimated by intrinsic functional connectivity. *Journal of neurophysiology* (2011).

[64] Demirtaş, M. *et al.* Hierarchical heterogeneity across human cortex shapes large-scale neural dynamics. *Neuron* **101**, 1181–1194 (2019).

[65] Rubinov, M., Kötter, R., Hagmann, P. & Sporns, O. Brain connectivity toolbox: a collection of complex network measurements and brain connectivity datasets. *NeuroImage* **47**, S169 (2009).

[66] Qu, Y. *et al.* A genetic algorithms for optimizing structural brain network across cognitive tasks. *2024 China Automation Congress (CAC)* 5210–5215 (2024).